Scientific Research Publishing

Advances in Aerospace Science and Technology, 2026, 11(2), 37-57
https://www.scirp.org/journal/aast
ISSN Online: 2473-6724
ISSN Print: 2473-6708

Numerical Investigation of Gust Response for a HALE Blended-Wing-Body UAV S-Duct Inlet

Zitong Huang, Yun Liu, Guoyi He, Zhixin Zhan

Department of Aeronautics and Astronautics, Nanchang Hangkong University, Nanchang, China
Email: 70641@nchu.edu.cn

How to cite this paper: Huang, Z.T., Liu, Y., He, G.Y. and Zhan, Z.X. (2026) Numerical Investigation of Gust Response for a HALE Blended-Wing-Body UAV S-Duct Inlet. *Advances in Aerospace Science and Technology*, **11**, 37-57.
https://doi.org/10.4236/aast.2026.112003

Received: March 9, 2026
Accepted: April 19, 2026
Published: April 22, 2026

Abstract

The dorsal S-duct inlet of a HALE blended wing body UAV faces complex unsteady disturbances during operation. This study numerically investigates its aerodynamic response to gust excitations. Using CFD, we analyzed the effects of angle of attack, gust ratio, frequency, and gust type on total pressure recovery and distortion index. Results reveal significant hysteresis in performance recovery post-gust. Increasing angle of attack amplifies response fluctuations, with recovery variation reaching 4.37% at 8˚ AoA. Gust ratio governs response magnitude, while frequency modulates it through spatial wavelength effects. Sinusoidal gusts induce more intense cyclical variations than 1-cos gusts. The exit flow field evolution shows strong phase-coupling with gust excitation. These findings elucidate the unsteady flow mechanisms and provide essential insights for dynamic stability evaluation of such inlets under realistic atmospheric conditions.

Keywords

HALE UAV, S-Duct Inlet, Gust Response, Unsteady Aerodynamics

1. Introduction

With the background of modern warfare gradually moving towards the direction of informatization and intelligence, High-Altitude, Long-Endurance Unmanned Aerial Vehicle (HALE UAV) has become an important means in realizing the control over information. Due to its strong combat endurance, wide-area reconnaissance and surveillance capability, and low observability as compared to conventional aircraft, HALE UAVs are becoming the focus of nations' aerospace development efforts. The blended wing body layout (lack of traditional horizontal and vertical tails, and high degree of integration between the wing and fuselage) is considered to be the most desired aero configuration for fulfilling the optimal

performance demands of HALE UAVs due to its extremely high L/D that offers superior aerodynamics effectiveness, while the exterior smooth, continuous curves give it better stealth qualities.

However, there are also some new problems that come with a blended wing body design such as how to install the engines on this type of aircraft. For traditional airplanes, the inlet can be installed and designed to a certain degree of freedom independently, taking advantage of fuselage or wings; while the lack of a conventional fuselage or empennage, which creates an extremely confined, relatively flat and highly integrated interior cavity. To achieve low observability, it is desired that a portion of the radar wave incident from in front of the aircraft does not directly illuminate the high reflectance compressor blades on the engine. a dorsal mounted inlet has been the mainstream choice of an inlet for blended wing body configuration. The dorsal inlets usually have a very high offset, aggressively curved S-duct between the dorsal intake and an engine mounted in the mid-to-aft part of the airframe which provided the required space for turning and guiding the incoming flow.

The first one concerns the unique location of the inlet. It does not reside in a clean freestream but it is embedded into the viscous boundary layer developed on top of the airframe. The ingestion of low energy, high-turbulence BL-flow seriously deteriorates the internal flow quality. Shock waves might appear upstream of the inlet under transonic/supersonic flying condition; shock/boundary-layer interactions with complicated airframe BL could even cause flow separation, which may cause inlet surge and/or engine instability.

Second, the extreme internal space constraints. The flattened internal architecture of the blended wing body configuration necessitates a "short and highly curved" duct with large centerline curvature and limited diffusion length. This severely restricts the physical space available for smooth flow deceleration and turning, posing substantial challenges for flow control and duct shaping, while simultaneously requiring accommodation of structural load paths and equipment systems layout.

Thirdly, the complexity of full-aircraft dynamics coupling. The blended wing body configuration has a relatively small static stability margin on both the longitudinal axis and the course axis, which makes it more susceptible to aerodynamic turbulence and gusts disturbance; tends to produce larger-amplitude, higher-frequency attitude fluctuations. The inlet is a first stage in a propulsion system and it's inlet condition changes as per the orientation (attitude) of complete aircraft, which vary in time due to aircraft motion. These time-varying inlet conditions are coupled to the inherent unsteadiness of the internal flow field inside the S-duct, which could potentially result in unsteady flow phenomena not revealed through a standard steady analysis, with the direct implication on general aviation safety, and on aircraft mission success.

So far, there are many comprehensive studies about the parametric design method, the static aerocharacteristics analysis of and optimization for the more

common S-duct type inlets which have comparatively well-established design paradigms. Nevertheless, for the special case of blended wing body configuration, there are still lack of systematical and comprehensive study on integrated, conformal inlet and fuselage geometry design methods; transient aerodynamic response and performance adaptation phenomena occurring during maneuvering conditions—such as wind gusts. Rapid gust induced transients in attitude and local flow fields of an aircraft can drive the inlet to severe operating states, such as high-incidence ingestion or strong crossflow, over a very short time period to cause abrupt performance degradation or instantaneous flow unsteadiness. Such a dynamic coupling process presents a key gap which are inadequately covered by traditional quasi-steady design and assessment criteria.

The design methods for conventional layout inlets have long attracted extensive attention in academia, with numerous scholars conducting systematic research in this area. Lee C C *et al*. [1] first proposed a design method for S-shaped inlets characterized by large offset and short diffuser features, defining the centerline type and cross-sectional area variation, which laid the theoretical foundation for subsequent developments in this field. Wei-Li Zhang *et al*. [2] extended this modeling approach to achieve the automatic generation of three-dimensional diffuser duct structures. Li Dawei *et al*. [3] drew on Lee's research approach to innovatively explore cross-sectional variation patterns and successfully applied them to the design of a dorsal S-shaped inlet with large offset and short diffuser features. Tu Qiuye *et al*. [4] introduced geometric constraints for S-shaped inlets while adopting the centerline variation pattern defined by Lee, proposing a polynomial-based centerline construction method that expanded the design space of centerlines and established nine typical centerline models based on inflection point locations. Guo Rongwei *et al*. [5] [6] conducted systematic design research on short S-shaped inlets for missile applications, comprehensively elaborating on the computer-aided design process and developing practical S-shaped inlets suitable for missile platforms. Additionally, scholars such as Tindell R H [7] and Mayer D W [8] further explored S-shaped inlet design methods, each proposing corresponding optimization strategies and design specifications.

In the design of inlet and exhaust systems with complex configurations, existing methods are mostly based on conventional configurations, combined with the irregular characteristics of inlet and outlet shapes, to develop corresponding cross-sectional transition generation techniques. Although research on inlet and exhaust systems with various non-circular cross-sections remains limited, some exploratory studies have achieved preliminary results. Zhou Huichen *et al*. [9] proposed a cross-sectional transition and generation method based on curvature control, supporting smooth transitions from complex inlet cross-sections to circular cross-sections, enabling efficient integrated modeling of complex inlet shapes, which was applied in the design of the X-47A slit inlet integrated with the forward fuselage. Gan Wenbiao *et al*. [10] focused on the conformal inlet of a flying-wing unmanned aerial vehicle, reconstructing the polynomial representation of the cor-

responding curves by referencing the centerline and cross-sectional area variation method proposed by Lee C C, achieving parametric design of the S-shaped inlet and conducting optimization studies in the conformal layout context. Li Yuefeng *et al*. [11] similarly built on Lee's approach, introducing super-ellipse equations for cross-sectional control, completing transitional designs from various inlet cross-sections—including rectangular, circular, rhomboidal, and elliptical shapes—to circular outlets, thereby validating the feasibility of this strategy for connecting non-circular cross-sections.

Regarding the analysis and evaluation of aerodynamic characteristics, relevant studies have provided important support for further understanding the internal flow mechanisms and performance evolution of S-shaped inlets. Byung Joon Lee *et al*. [12] conducted optimization design research on S-shaped subsonic inlets based on NURBS curves. Aniket Aranake *et al*. [13] proposed an automated computational method for dual S-shaped subsonic diffusers and summarized simplified design criteria for reducing outlet distortion based on experimental results. Zhang Z K *et al*. [14] introduced the adjoint method into the design optimization process of S-shaped inlets. In terms of numerical simulation and aerodynamic characteristic analysis, Lee B J *et al*. [15] performed numerical simulations and experimental comparisons on models incorporating S-shaped diffusers using various turbulence models, showing that the SST model provides higher prediction accuracy for flow separation. Weske J R [16] systematically analyzed the velocity distribution and total pressure loss at the inlet exit. Guo *et al*. [17] experimentally studied the secondary flow characteristics inside S-shaped inlets; Goldsmith [18] focused on the evolution of flow distortion within inlets. These studies have laid a solid theoretical and technical foundation for revealing inlet flow mechanisms, model construction, and performance evaluation. However, for flying-wing unmanned aerial vehicles under conformal integrated design constraints, the inlet cross-section exhibits complex and irregular characteristics. This imposes higher demands on inlet design methods and raises new critical issues: how to effectively leverage the internal flow potential of the inlet and exhaust system while meeting stealth requirements, thereby achieving comprehensive improvements in overall aircraft aerodynamic performance.

In this context, in order to address these issues, the objective of this paper is to conduct a step-by-step analysis of the joint optimization approach, steady aerodynamic characteristics, as well as basic dynamic properties—in particular, gust response behavior—of an upper-back conformal S-duct inlet of a high-altitude long-endurance (HALE) blended wing body unmanned aerial vehicle (UAV).

2. Numerical Simulation Methodology

The fundamental governing equations consist of the conservation of mass, linear momentum, angular momentum, and energy.

$$\frac{\partial \rho}{\partial t} + \nabla \cdot (\rho \boldsymbol{v}) = 0 \tag{1}$$

$$\frac{\partial(\rho \boldsymbol{v})}{\partial t}+\nabla\cdot(\rho \boldsymbol{v}\otimes \boldsymbol{v})=\nabla\cdot\boldsymbol{\sigma}+\boldsymbol{f}_b \tag{2}$$

$$\boldsymbol{\sigma}=\boldsymbol{\sigma}^{\mathrm{T}} \tag{3}$$

$$\frac{\partial(\rho E)}{\partial t}+\nabla\cdot(\rho E\boldsymbol{v})=f_b\cdot\boldsymbol{v}+\nabla\cdot(\boldsymbol{v}\cdot\boldsymbol{\sigma})-\nabla\cdot\boldsymbol{q}+S_E \tag{4}$$

In this work, we use the FVM to discretize the set of differential equations that solve the conservation equation in terms of mass for fluid flow, where we have defined the momentum, and the energy:

$$\frac{\partial}{\partial t}\int_V \rho \mathrm{d}V+\oint_A \rho\boldsymbol{v}\cdot\mathrm{d}\boldsymbol{a}=\int_V S_u\mathrm{d}V \tag{5}$$

$$\frac{\partial}{\partial t}\int_V \rho\boldsymbol{v}\mathrm{d}V+\oint_A \rho\boldsymbol{v}\otimes\boldsymbol{v}\cdot\mathrm{d}\boldsymbol{a}=-\oint_A p\boldsymbol{I}\cdot\mathrm{d}\boldsymbol{a}+\oint_A \boldsymbol{T}\cdot\mathrm{d}\boldsymbol{a}+\int_V \boldsymbol{f}_b\mathrm{d}V+\int_V S_u\mathrm{d}V \tag{6}$$

$$\frac{\partial}{\partial t}\int_V \rho E\mathrm{d}V+\oint_A \rho H\boldsymbol{v}\cdot\mathrm{d}\boldsymbol{a}=-\oint_A \boldsymbol{q}\cdot\mathrm{d}\boldsymbol{a}+\oint_A \boldsymbol{T}\cdot\boldsymbol{v}\cdot\mathrm{d}\boldsymbol{a}+\int_V \boldsymbol{f}_b\cdot\boldsymbol{v}\mathrm{d}V+\int_V S_u\mathrm{d}V \tag{7}$$

where t is time, V is volume, $\boldsymbol{a}$ is the outward-pointing area normal vector, ρ is density, $\boldsymbol{v}$ is the fluid velocity vector, $\otimes$ is the velocity of the control volume surface, $\boldsymbol{f}_b$ is the resultant of external body forces per unit volume (e. g., gravity, centrifugal force), $\boldsymbol{\sigma}$ is the stress tensor, E is the total energy per unit mass, $\boldsymbol{q}$ is the heat flux vector, S_E is the energy source per unit volume, p is pressure, $\boldsymbol{I}$ is the unit tensor, $\boldsymbol{T}$ is the viscous stress tensor, H is the total enthalpy per unit mass, S_u is the mass source term。

2.1. Gust Generation

Gust response analysis needs to be carried out at detailed design stage for any aircraft to meet airworthiness certification standards.

This calculation is based on a definition of an atmospheric gust model from the airworthiness regulations like the Federal Aviation Regulation, CCAR-25 (China Civil Aviation Regulation) regulations, the vertical continuous gust model is usually taken as the discrete gust load analysis model. In them, the "1-cos" discrete gust model, which has been adopted as the most common standard model.

To conduct gust response calculation in time domain, the mathematical representation of the gust model should be derived in the time domain at first. The representation determines exactly what kind of form will the gust velocity change has and is also the input foundation driving all dynamics response analyses. Eq.(8) shows the corresponding "1-cos" gust's time domain representation.

$$U_g(t)=\frac{U_{ds}}{2}\left[1-\cos\left(\frac{2\pi V}{H}t\right)\right] \tag{8}$$

Equation (9) is the time-domain expression for the sinusoidal ("sin") gust.

$$U_g(t)=\frac{U_{ds}}{2}\sin\left(\frac{2\pi V}{H}t\right) \tag{9}$$

where: U_g is the vertical gust velocity, U_{ds} is is the gust gradient distance

(characterizing the gust wavelength), V is the aircraft velocity, t is time.
The gust ratio GR is defined as follows:

$$GR = \frac{V}{U_\infty} \tag{10}$$

where V denotes the gust amplitude and U_∞ represents the free-stream velocity.

2.2. Case Validation

The internal flow field of an S-shaped inlet is complex. While appropriate numerical simulation methods can enhance simulation accuracy, it is challenging for any single numerical approach to guarantee absolute precision in the results. Different computational methods may lead to variations in the outcomes. Therefore, before conducting in-depth research and analysis, it is necessary to validate the chosen computational method to ensure its reliability.

The physical model of the S-shaped inlet used for validation is derived from the reference "Experimental Study on Flow Control Technology for S-Shaped Inlets" [14]. The centerline shape of this model is as follows:

$$Z_{cl} = -\Delta Z_{cl}\left[1-\cos\left(\pi\frac{X_{cl}}{L}\right)\right], 0 \le X_{cl} \le L \tag{11}$$

where: X_{cl}, Z_{cl} are the x, z coordinates of the centerline; ΔZ_{cl} is the offset distance from the centerline; L is the length of the inlet.
The radius distribution of the inlet (measured perpendicular to the centerline) is as follows:

$$\frac{R-R_i}{R_{ef}-R_i} = 3\left(1-\frac{X_{cl}}{L}\right)^4 - 4\left(1-\frac{X_{cl}}{L}\right)^3 + 1 \tag{12}$$

where: R_i is the radius at the throat; R_{ef} is the radius of the inlet exit cross-section.

The geometric parameters of this inlet model are as follows: throat radius $R_i = 0.0744$ m, exit radius $R_{ef} = 0.088$ m, total length $L = 0.5282$ m, and offset distance $\Delta Z_{cl} = 0.1584$ m. A bell-shaped lip with a length equal to one times the throat radius is designed at the inlet entrance.

The inlet boundary condition of the S-shaped duct is set as a pressure inlet. For comparison with experimental results, the inflow conditions are configured to match the experimental free-stream velocity $V = 60$ m/s, with a total temperature of 298 K and a total pressure of 101,000 Pa at the inlet. The angle of attack is $\alpha = 8^\circ$ and the sideslip angle is $\beta = 0^\circ$. The outlet of the S-shaped inlet is set as a pressure outlet with a specified back pressure, while the walls of the S-shaped duct are treated as no-slip walls. An unstructured mesh is employed for the computational domain, with boundary layer refinement near the walls.

Before conducting numerical simulations, it is essential to determine the appropriate mesh size. In this study, three grids with varying densities were designed

to conduct a grid independence study. The specific grid cell counts are listed in Table 1.

Table 1. Mesh size.

	Mesh1	Mesh2	Mesh3
mesh size (ten thousand)	1523	1842	2132

The CFD method described earlier was employed to simulate the S-shaped inlet, and the computational results obtained from the three grids were compared with experimental data. The comparative metrics selected are the total pressure recovery coefficient and the distortion index, which are defined as follows:

$$\sigma = \frac{p_{t2}}{p_{t\infty}} \tag{13}$$

$$DC_{60} = \frac{p_{av} - (p_{\min})_{60}}{q_{av}} \tag{14}$$

Taking the center point of the inlet exit plane as the reference point, p_{t2} is the average total pressure at the inlet exit, $p_{t\infty}$ is the free-stream total pressure upstream of the inlet entrance, $(p_{\min})_{60}$ is the minimum average total pressure within a 60˚ angular range, q_{av} is the average dynamic pressure at the exit, and p_{av} is the average total pressure at the exit.

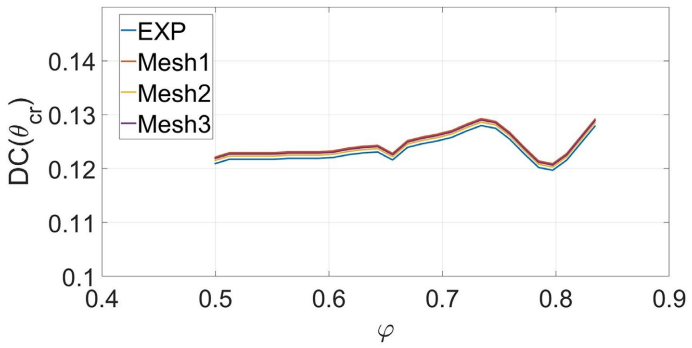

Figure 1. Variation of distortion index with mass flow coefficient.

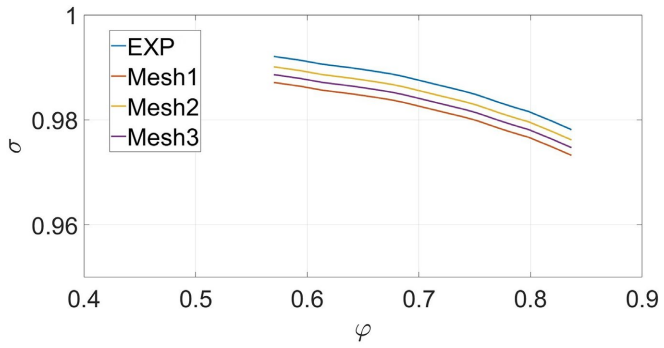

Figure 2. Variation of total pressure recovery coefficient with mass flow coefficient.

As shown in Figure 1 and Figure 2, based on the comparison, the relative error between the experimental total pressure recovery coefficient and the simulation result is 0.5%, while the relative error for the distortion index is 1.0%. In summary, the methodology employed in this study can effectively simulate the flow field of the S-shaped inlet.

2.3. Computational Model and Boundary Conditions

This study employs the commercial CFD software Star-CCM+ as the solver. For steady flows, an implicit steady solver is adopted for steady-state computations; for unsteady gust responses, a first-order implicit unsteady formulation is utilized. The SST k-ω turbulence model is selected to ensure resolution accuracy in regions with adverse pressure gradients. Spatial discretization is performed using a second-order upwind scheme, while transient terms are handled with a second-order implicit formulation.

The research object here is the intake gust response, the geometrical size of the physical model is that the fuselage length is 13.5 m and the wing span is 25.983 m. The set-up flowfield is rectangular flowfield whose dimension is 260 m (length) × 200 m (width) × 100 m (height), and the nose of the model is located at 60m away from the flowfield inlet, at a distance of 50 m from the upper and lower boundary, as well as 100 m away from the left and right boundaries. The model is presented in Figure 3.

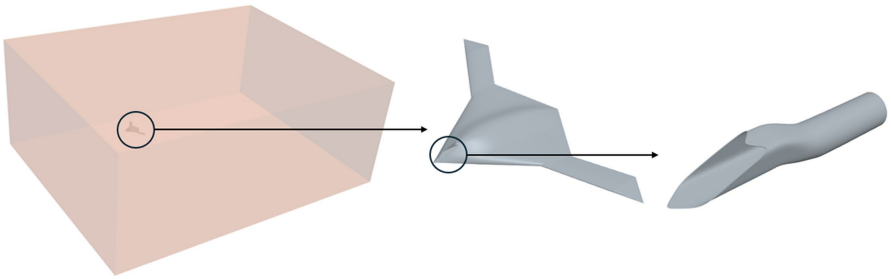

Figure 3. Computational model.

The inlet is set as a velocity inlet, the outlet as a pressure outlet, the aircraft surfaces as no-slip walls, and the remaining faces are also set as pressure outlets. The distribution of these boundary conditions is shown in Figure 4.

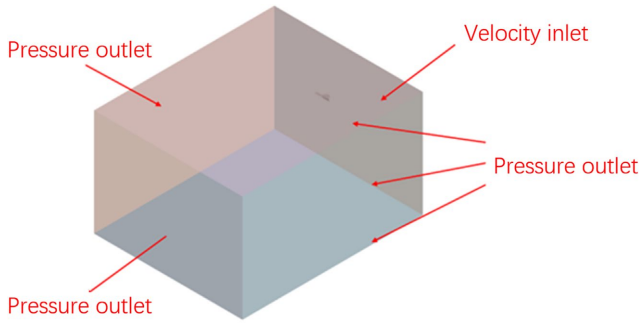

Figure 4. Computational domain.

2.4. Grid Independence Verification

The mesh quality and the mesh quantity have a great influence on the calculation result and efficiency of the calculation program. In order to verify that the meshing method adopted in this paper can meet the calculation requirement, a grid independency test has been carried out. In the present investigation for that purpose we have used three series of different mesh refinements (coarse, medium, and fine—were created. The simulations for the same boundary conditions have been conducted on all of them. In particular, at the working point $Ma = 0.71$; $H = 5$ km are used three meshes sets composed by about 35.25 millions, 17.76 million, and 10.54 million elements was verified. The verification results are as Figure 5 shows.

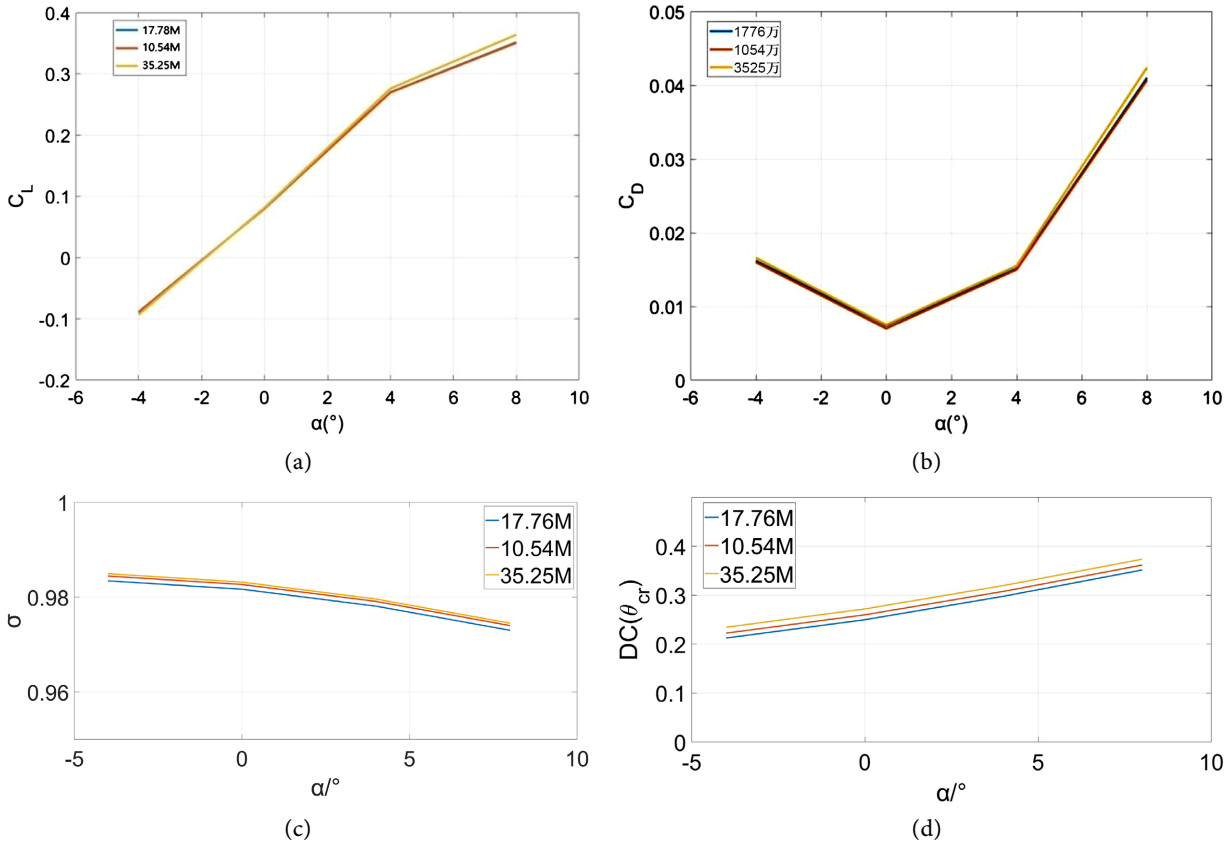

Figure 5. Grid independence study validation. (a) Variation of lift coefficient with varying mesh counts; (b) Variation of drag coefficient with varying mesh counts; (c) Total Pressure recovery coefficient; (d) Distortion index.

The lift coefficient and drag coefficient change almost not at all with increasing element quantity among the three mesh sets. And the deviation of both the lift coefficient and drag coefficient among the three sets is less than 5%. It can be seen that the mesh resolution has enough ability to reflect the details of the flow field and satisfies the accuracy requirement of numerical simulation.

Therefore, we chose the mesh scheme which has about 17.76 million elements as the final study. The reason is that it can get a better compromise in terms of calculation speed and precision. It not only improves the computing stability but

also ensures the accuracy and reliability of the simulation results. Then, for this mesh, the boundary layer is solved by using 30 layers. The thickness of the first layer near the wall is 9.396×10^{-6} m, the total boundary layer thickness is 8.129×10^{-2} m. The number of elements in the final mesh is 17.76 M.

3. Intake Gust Response

3.1. Intake Response under Steady Inflow

The operating conditions for the steady ingesting inflow case have been fixed as mentioned in the following Table 2 so that we can investigate how does the aerodynamic performance of the UAV's inlet changes with change in angle of attack, and to systematically study the aerodynamics behavior of the over-wing mounted intake in case of a blended-wing-body UAV with a uniform inflow, so as to give some benchmark results which can be compared to future investigations in case of a gust disturbance. The main studied parameters are the exit Mach number, total pressure recovery coefficient and total pressure distortion index in this paper.

Table 2. Calculation conditions table.

Ma	*H*(km)	α (˚)
0.6	6	−4, 0, 4, 8

The Total Pressure Recovery Coefficient can be defined as a ratio between the mean total pressure on the exit of the intake and the freestream total pressure upstream from the inlet of the intake, denoted as σ:

$$\sigma = \frac{p_{t2}}{p_{t\infty}} \tag{13}$$

The non-uniformity of the total pressure on the exit plane of the intake, known as distortion, can be measured by a quantity called Distortion Index, denoted by $DC(\theta_{cr})$, and it can be defined as:

$$DC(\theta_{cr}) = \frac{p_{av} - (p_{\min})_{\theta_{cr}}}{q_{av}} \tag{14}$$

where: $(p_{\min})_{\theta_{cr}}$ is the minimum sector average total pressure within the θ_{cr} sector, θ_{cr} is the critical distortion angle (in this paper, is $\theta_{cr} = 60^{\circ}$ selected),; q_{av} is the average dynamic pressure,; p_{av} is the average total pressure across the entire exit plane.

The overall pressure recovery coefficient (σ) and inlet distortion index ($DC(\theta_{cr})$) for the developed intake at varying angles of attack, are shown in the following picture.

As shown in Figure 6, with the increase of the angle of attack, the total pressure recovery coefficient decreases and the distortion index is increased accordingly. It can be seen that there is an overall decline on the aerodynamic performance for the intake at larger angles of attack, with increased flow loss, and reduced uni-

formity of the exiting flow.

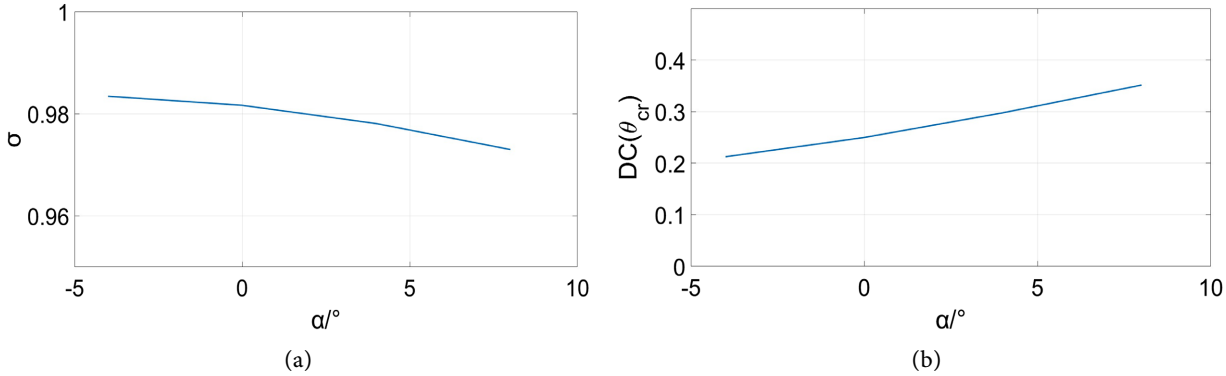

Figure 6. Total pressure recovery coefficient and distortion index under steady-state conditions. (a) Variation of total pressure recovery coefficient with angle of attack; (b)Variation of distortion index with angle of attack.

The change in the distribution of pressure contours can also indicate the mechanism of field flow behind such a performance change, as indicated by the following **Figure 7**, with a growing AoA, the high pressure zone in the middle of the intake exit plane is greatly compressed, and it's pressure maximum is slowly decreasing at the same time as the low-pressure area above the plane keeps expanding. This immediately translates into a lower overall total pressure level at the exit (*i.e.* lower total pressure recovery coefficient), as well as higher pressure gradient over the plane (*i.e.* a deterioration (increase) of the distortion index), and thus explains the inherent degradation of intake performance with angle of attack, from the viewpoint of flow field structure. We can also notice that with an increasing angle of attack, there is a corresponding increase in the inlet velocity of the incoming flow. It will further enhance the compression effect and the tendency of boundary layer separation, which plays an important role on deteriorating total pressure recovery performance, as well as increasing flow distortion.

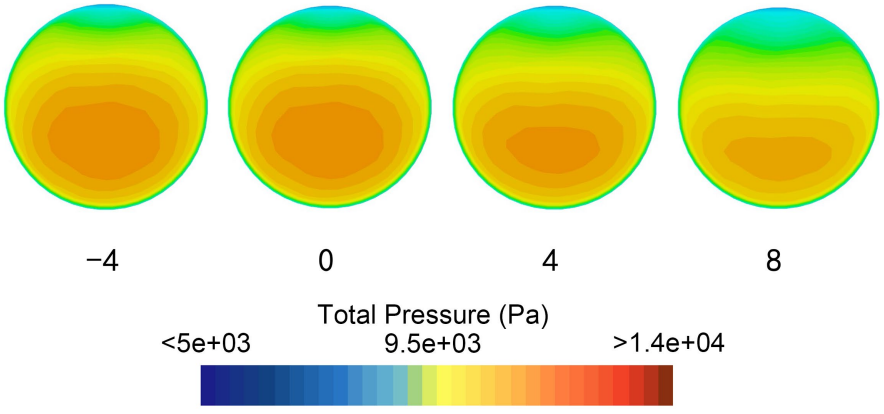

Figure 7. Intake exit pressure contour.

As shown in **Figure 8**, the streamline plot indicates that main stream inside the intake is remained attached for all of the calculated range of angle of attack, with

no large-scale flow separation occurring. As the angle of attack increases however, more low-energy boundary layer flow from the forebody is ingested into the intake, and it plays a much stronger role. This low-total-pressure flow entrainment directly dilutes the total pressure level at the exit plane and decreases the total pressure recovery coefficient. Meanwhile, the increased mixing with, and interaction of this low energy flow with the main core stream increases the pressure gradient in the exit plane, which manifests itself by increasing of a distortion index. This behavior also makes physical sense given what we see from the pressure contours—the narrowing of the high pressure region and widening of the low pressure region—together explain how the increased AoA causes a degradation to intake performance through its effects on internal flows.

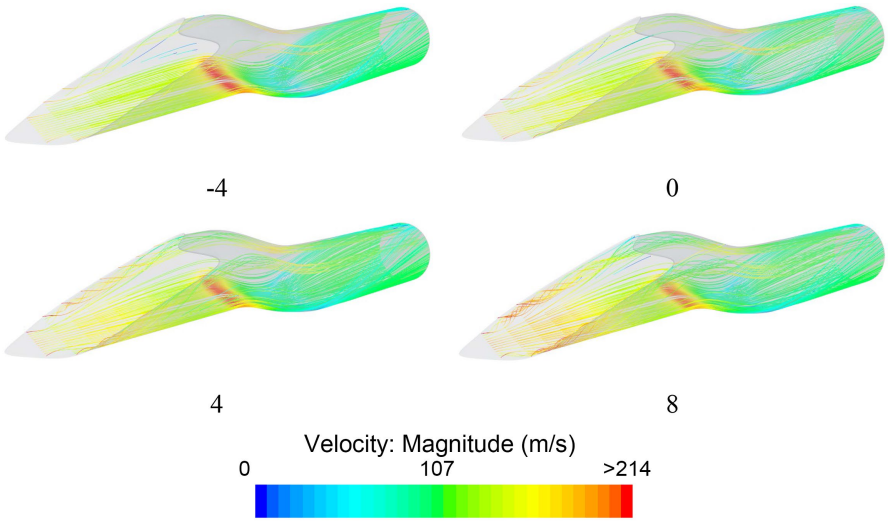

Figure 8. Streamline plots at different angles of attack.

3.2. Intake Response under Unsteady Inflow

The above-mentioned steady state situations have been analyzed to reveal how systematically the aircraft attitude (angle of attack) affects the intake performance, but, in real flights, atmospheric turbulence/gust is inevitable source of unsteady disturbance. The disturbance subjects the intake inlet to extremely fluctuated, non-homogeneous boundary condition in time. This transitory inlet condition will not only cause transitory flow separation and reattachment within the inlet, but it will also more seriously, propagates pressure perturbations downstream that can endanger the operating margin of the engine.

Thus, a steady-state-only assessment of its performance cannot be sufficient for representing the intake's applicability in real, complex environments. To explore its dynamic disturbance rejection ability, as well as the transient performance of its flow field quality, unsteady numerical simulation for the whole intake in case of normal gust excitation would be performed. The main research objective is to investigate the multi-dimensional dynamic characteristics of intake performance parameter (total pressure recovery coefficient and distortion index) caused by gust

disturbance, examining in depth how each one of the following factors influences:

Different Mean Angles of Attack: Studies the variation in the intake's sensitivity and stability to dynamic disturbances under different baseline flight attitudes.

Gust Frequency Variation: Studies the dependence on the perturbation timescale (from slow low frequency fluctuations, up through fast high frequency transients), with respect to the resulting interior flow response in the inlet.

Varying Gust Strengths (Gust Ratio): The effect of gust magnitude on the extent of variation in control response variables, as well as on the severity at which a stall condition occurs.

Different Gust Types (Sinusoidal Gust, 1-cos Gust): Compares the differing mechanisms by which disturbances with distinct spatial-temporal distribution characteristics affect the transient loads and performance degradation of the intake.

With an integrated study on the aforementioned high-dimensional parameters space, this paper is intended for revealing systemically the law about the development of the intake performance under the unsteady inflow, provides detailed data support and theoretical basis to the dynamic stability evaluation and robustness design of.

The purpose of present work is to improve the evaluation of the operating envelope of the intake in terms of dynamics so as to provide necessary foundation on predicting the performance and designing the stability of the intake at unstably flying states.

The calculation conditions for the intake under gust environments are as follows Table 3.

Table 3. Calculation conditions under gust environment.

Variable	Fixed Parameters	Comparative Parameters
Different Angles of Attack	Gust Type: Sinusoidal. Frequency: 5 Hz; Gust Ratio: 0.1	−4˚, 0˚, 4˚, 8˚
Different Gust Ratios	Gust Type: Sinusoidal. Frequency: 5 Hz; Angle of Attack: 0˚	0.05, 0.1, 0.15
Different Frequencies	Gust Type: Sinusoidal. Angle of Attack: 0˚; Gust Ratio: 0.1	1 Hz, 5 Hz, 10 Hz
Different Gust Types	Angle of Attack: 0˚; Frequency: 5 Hz; Gust Ratio: 0.1	sin, 1-cos

The gust response results of the intake are as follows.

The curves in Figure 9 and Figure 10 show the transient response characteristic of main aerodynamics parameter of intake with different angle-of-attack, and on total pressure recovery coefficient: in a region of small angle of attack values where the influence of the incoming gust disturbance onto the inner flow pattern is rather low. The mean-value of total-pressure-recovery-coefficient is still relatively large and has a small amplitude of fluctuation, which presents a relative-fluctuation level as 2.05%, 0.81%, and 2.39%, respectively. The variations are clearly well

temporally correlated to the gust velocity wave shape suggesting that at these conditions the overall evolution of the pressure recovery is mainly driven by the local variations of the inflow speed.

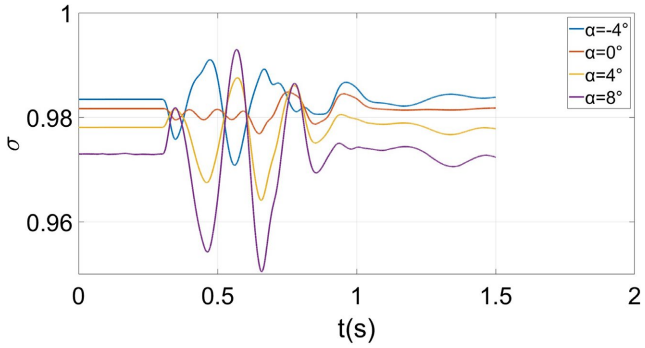

Figure 9. Total pressure recovery at different angles of attack.

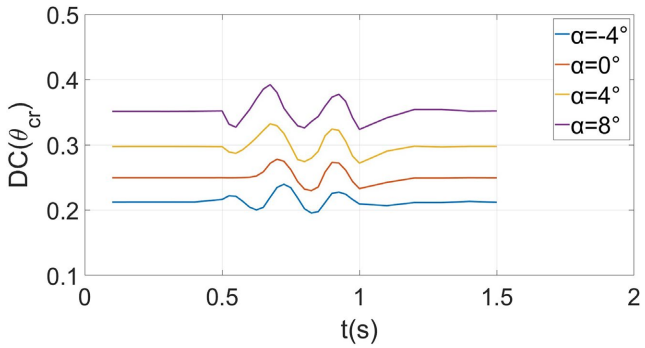

Figure 10. Distortion index at different angles of attack.

With increasing angle of attack, intensified flow separation and boundary layer distortion make the effect of gust disturbance much more pronounced. In a large angle-of-attack regime, the standard deviation value of overall pressure recovery factor is increased up to 4.37%. It is also worth mentioning here that there is higher fluctuation level for 8o AoA as compared to other two low AoAs which implies that with increasing AoA, the flow becomes less stable.

For the distortion index itself, it can be seen from the dynamic response also has the feature of following with respect to the incoming gust, but there is an obvious difference in terms of angle of attack: the amplitude of the distortion index's vibration at large angles of attack is much larger than that of small angles of attack. This result again proves that a larger angle of attack will deteriorate the aerodynamic performance of the intake, and it also intensifies the unsteady features of the flow non-uniformity. So it has larger effect to the steady running of lower stream engine.

Noteworthy also is that after passing the gust, it can be clearly observed that the total pressure recovery coefficient still exhibits fluctuations after 1 second. This phenomenon reveals that the reconstruction and stabilization of the internal flow field within the inlet require a certain amount of time, and the flow recovery lags

behind the external free-stream disturbances. The fact indicates that the reorganization/stabilization process of the internal flow field inside the intake takes some time to complete, *i.e.*, the return to its aerodynamic condition is delayed with respect to the end of the external perturbation.

As shown in Figure 11 and Figure 12, at various gust ratios in excitation conditions, the intake's dynamic responses features show obvious rules: The transient trend for the overall pressure recovery coefficient as well as the distortion index is identical, but that their dynamic response amplitudes change dramatically as a function of the gust magnitude (gust ratio). In particular, higher gust ratio represents stronger input of dynamic pressure disturbance that increases greatly the unsteady characteristics of the internal flow inside the intake as well as the aerodynamic/structural coupling effect; thus, causing the sharp increase in the oscillation amplitude of both the total pressure recovery coefficient and the distortion index. On the other hand, at low gust ratio condition, the energy of the incoming flow perturbation is smaller, leading to a small modulation for the flow state; and so do the amplitude of the dynamical fluctuations of the above quantities.

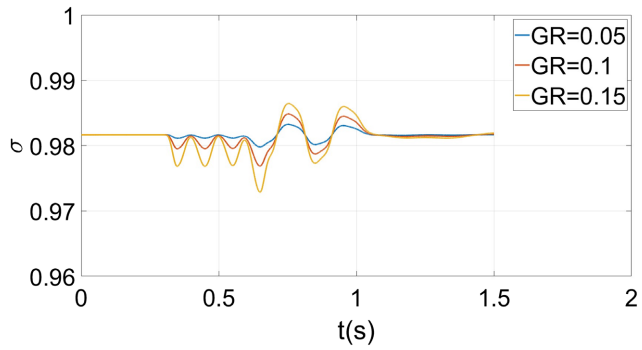

Figure 11. Total pressure recovery at different gust ratios.

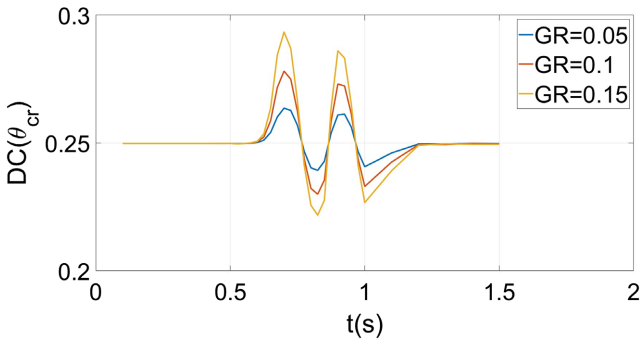

Figure 12. Distortion index at different gust ratios.

This also means that the gust ratio determines the magnitude of the dynamic response gain of this system, namely it controls how much the response of the intake will amplify an incident flow disturbance and when this becomes unstable.

As shown in Figure 13 and Figure 14, in the response to the gust excitation with various frequency, although the evolution trend of total pressure recovery

coefficient and distortion index in the time domain are quite similar, their response amplitudes are strongly dependent on the frequency. With an increasing excitation frequency, a decreasing gust wavelength is associated with it. In particular, since the wavelength of a 1 Hz and 10 Hz gust is about 189.6 m and 18.96 m, respectively. This discrepancy in wavelength is basically reflecting on the spatial scale of the flow perturbation: low frequency perturbations possess a large wavelength, leading to rather mild spatial velocity gradient; while the high frequency perturbations possess small wavenumbers, resulting in a much larger velocity gradient that reduces the adaptive adjustment and equilibration timescale of the flow structure against the perturbation. Therefore, at a high frequency excitation, the amplitudes of dynamic fluctuation of the two quantities (total pressure recovery coefficient and distortion index) have been greatly weakened.

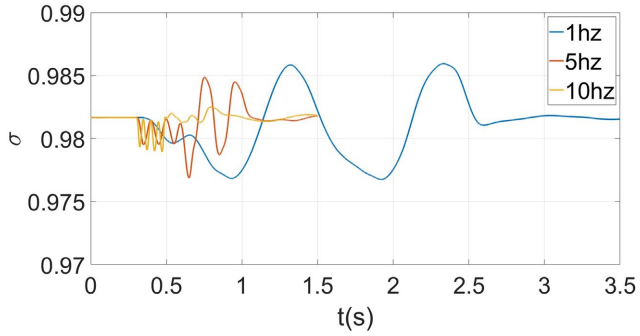

Figure 13. Total pressure recovery at different frequencies.

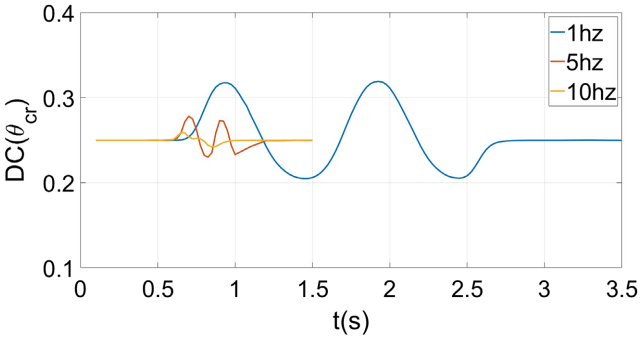

Figure 14. Distortion index at different frequencies.

As shown in **Figure 15** and **Figure 16,** the unsteady aerodynamic response under the excitation from different kinds of gusts shows obvious difference in modes for the intake. Under the 1-cos gust, without having a continuous vertical component of motion in its excitation cycle, has lesser degree of dynamic loading on the intake inlet flow field. Hence, it excites aerodynamical response of low frequencies, while both overall pressure recovery factor and distortion level have just one clear minimum in this course. On the contrary, the sinusoidal gust contains one full cycle of vertical velocity change. It induces more intense response because of its larger flow field excitation. During the same time period, the overall pressure

recovery coefficient presents evident valleys and peaks that lead to a more compact dynamic behavior.

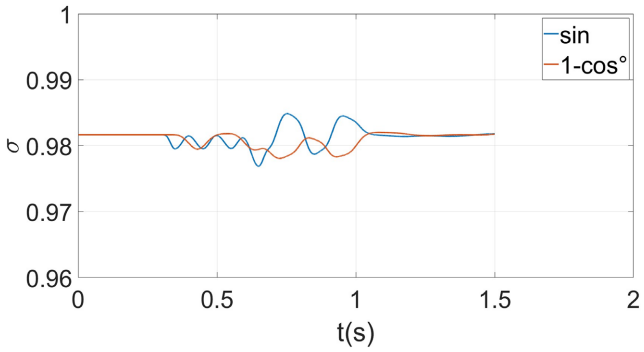

Figure 15. Total pressure recovery for different gust types.

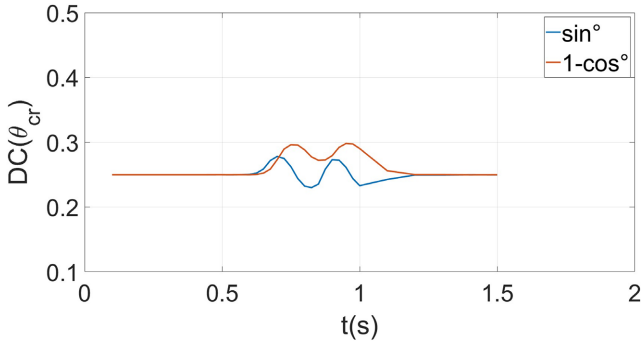

Figure 16. Distortion index for different gust types.

A further observation is that in the case of the 1-cos gust the instantaneous value of the total pressure recovery coefficient remains lower than its corresponding value obtained under the gust-free baseline state for most part of the time; indicating therefore that such an excitation form has a persistent attenuating effect upon the time-averaged performance of the intake. The dynamic evolution of the distortion index displays high synchronicity to that of the total pressure recovery coefficient, their patterns of change to be approximately similar. This together proves that there exists a good correlation between the inside non-steady flow field characteristics and aerodynamics performance of the intake under the disturbance of various gusts.

During the investigation on the influence from sinusoidal gust excitation, it is found that the total pressure recovery coefficient can, at some times to be higher than its steady state (gust free) level. This happens in the time when the gust has a vertical downwards component which means that instantaneous inflow disturbances with a certain orientation can, to some extent and for a limited time period to alleviate the flow condition in the intake and improve the total pressure recovery performance. This result indicates that the impact of gusting on the inlet can be non-negative in some cases, with some relationship between the directional character of the gust and transient aerodynamic gain.

Figure 17 shows the pressure contour distributions on the exit plane during one full cycle of the gust (Sinusoidal gust, 5 Hz, Gust Ratio 0.1). It can be seen from the pressure contours that the overall pressure field pattern changes as the gust progresses through its cycle: During the early period (first ¼ cycle), the higher the gust strength is, the smaller area of pressure peak appears to be. Second 1/4-cycle: With the weakening of the gust, during the second half of this 1/4-cycle the HP region grows again with a simultaneous large growth of its pressure maximum.

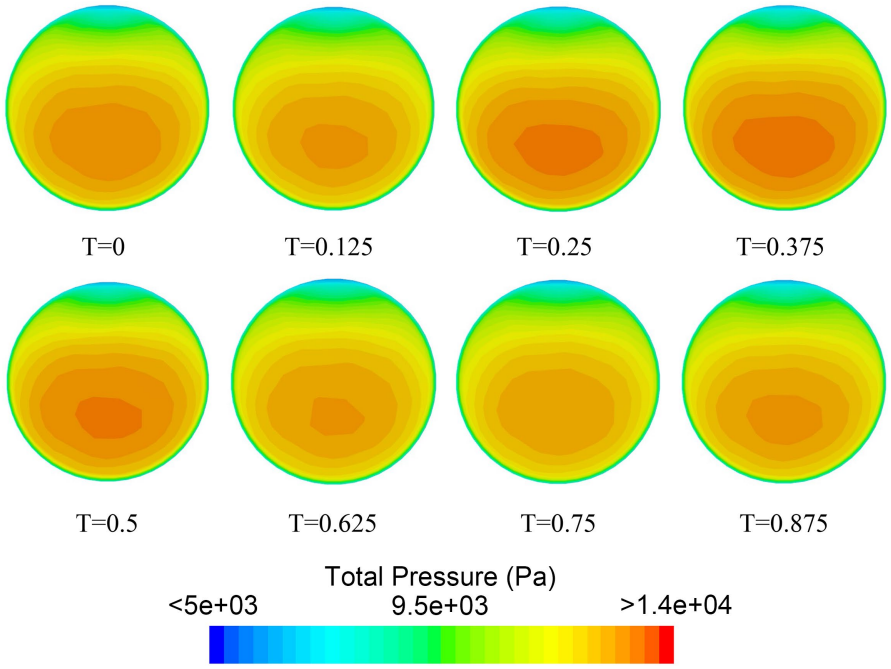

Figure 17. Exit pressure contours at different time instants (Condition: Sinusoidal gust, 0˚ angle of attack, 5 Hz, Gust Ratio 0.1).

4. Conclusions

In this paper, we use a computational model to conduct systematic analysis on the unsteady aerodynamic response characteristics for an intake under excitation from different gusts with varied parameters (angle of attack, gust ratio, frequency and gust type) to reveal the dynamic flow mechanism and the underlying physics. The major findings include:

The intake's recovery under gust excitation shows a large hysteresis feature. Even when the gust perturbation disappears, key parameters like the total pressure recovery coefficient still fluctuate, showing that the reorganization and stabilization of the internal flowfield are characterized by pronounced transients, and the response of the state recovery of the system is delayed compared to the external excitation.

The angle of attack also influences the response intensity. The influence of gust disturbance at small angles of attack is limited, leading to lower fluctuating am-

plitude values for the overall pressure recovery coefficient (≤2.39%) and being mainly regulated by transient variations on the incoming flow velocity. With increasing angle of attack, due to stronger flow separation effect as well as the increase of aerodynamic coupling effects, the amplitude values of dynamic fluctuations for total pressure recovery coefficient and distortion index are greatly increased (e. g., reaching 4.37% at 8o angle of attack), which indicates that the flow is less stable in this condition (high angle of attack) for the intake.

The gust ratio (excitation intensity) directly controls the magnitude of the dynamic response. High gust ratios induce high levels of dynamic pressure disturbance, which greatly enlarges the oscillation amplitudes of the total pressure recovery coefficient and distortion index, respectively. On the contrary, low-gust-ratios because they have lower disturbance-energy values produce corresponding lower amplitudes of system responses. Although this tendency of response is identical for all these values of gust ratio, it can be seen that the magnitude changes show a great sensibility of the system concerning the level of excitation.

Gust frequency (excitation timescale) influences the response amplitude through spatial wavelength. Low-frequency gusts have longer wavelengths and gentler flow field velocity gradients, allowing the system more time to respond and equilibrate, which leads to larger dynamic fluctuation amplitudes. High-frequency gusts have short wavelengths and steep local velocity gradients, where enhanced flow inertial effects and shortened adaptive timescales cause significant attenuation in the fluctuation amplitudes of both total pressure and the distortion index.

The gust type (excitation mode) defines the physical make-up of the disturbance, as well as the ensuing response pattern. The 1 cos gust, that does not have the persistent vertical component, is less intense perturbation generating smaller frequency responses, and has persistently negative impact on mean values of performance. On the other hand, the sinusoidal gust (which covers an entire vertical velocity cycle) is a stronger perturbation which produces denser dynamics response at higher frequency with greater magnitude.

The evolution pattern of the exit flow field is consistent with the gust phase, which can be intuitively illustrated by the dynamic pressure contours showing that the size and magnitude of the high pressure zone are inversely correlated to the gust strength; namely, they shrink as the gust becomes stronger while they increase in both scope and pressure extrema if a weaker gust appears. Thus, we have an intuitive demonstration of how well coupled the external excitation and internal unsteady flow structure truly are.

In conclusion, the dynamic aerodynamic performance of the intake is due to the coupling effects of several parameters such as angle of attack, gust intensity, timescale, and excitation mode. The present work illustrates the influence patterns and physical mechanisms for every parameters, provides a useful foundation to evaluate and predict intake operation stability and performance development in the case of complicated unsteady flow-inlet.

Conflicts of Interest

The authors declare no conflicts of interest regarding the publication of this paper.

References

[1] Lee, C. and Boedicker, C. (1985). Subsonic Diffuser Design and Performance for Advanced Fighter Aircraft. *Aircraft Design Systems and Operations Meeting*, Colorado Springs, 14-16 October 1985, 3073. https://doi.org/10.2514/6.1985-3073

[2] Zhang, W., Knight, D.D. and Smith, D. (2000) Automated Design of a Three-Dimensional Subsonic Diffuser. *Journal of Propulsion and Power*, **16**, 1132-1140. https://doi.org/10.2514/2.5688

[3] Li, D.W., Zhang, Y.F. and Ma, L.D. (2006) Design and Numerical Analysis of Dorsal S-Shaped Inlet. *Journal of Propulsion Technology*, **27**, 61-65. (In Chinese)

[4] Tu, Q.Y., Hu, W.H. and Chen, J. (2013) Research on Centerline Equation Construction of S-Shaped Inlet and Its Influence. *Advances in Aeronautical Science and Engineering*, **4**, 376-380. (In Chinese)

[5] Wan, D.W. and Guo, R.W. (2004) Design and Experimental Investigation of an S-Shaped Inlet. *Journal of Nanjing University of Aeronautics & Astronautics*, **36**, 150-154. (In Chinese)

[6] Xie, L.R. and Guo, R.W. (2006) Design and Experimental Validation for a Missile S-Shaped Inlet with Overall Constraints. *Acta Aerodynamica Sinica*, **24**, 95-101. (In Chinese)

[7] Tindell, R.H. (1988) Highly Compact Inlet Diffuser Technology. *Journal of Propulsion and Power*, **4**, 557-563. https://doi.org/10.2514/3.23100

[8] Mayer, D., Anderson, B. and Johnson, T. (1998) 3D Subsonic Diffuser Design and Analysis. 34*th AIAA/ASME/SAE/ASEE Joint Propulsion Conference and Exhibit*, Cleveland, 13-15 July 1998, 3418. https://doi.org/10.2514/6.1998-3418

[9] Zhou, H.C., Tan, H.J. and Li, X.P. (2009) Design Method of Inlet with Complex Variable Cross-Sections. *Journal of Aerospace Power*, **24**, 1357-1363. (In Chinese)

[10] Gan, W.B., Zhou, Z., Xu, X.P., *et al.* (2014) Optimization Design and Analysis for S-Shaped Inlet. *Journal of Propulsion Technology*, **35**, 1317-1324. (In Chinese)

[11] Li, Y.F., Yang, Q.Z. and Sun, Z.Q. (2011) Design and Aerodynamic Performance Study of Su-per-Ellipse S-Shaped Inlet. *Computer Simulation*, **28**, 82-85. (In Chinese)

[12] Lee, B.J., Kim, C. and Rho, O. (2005) Optimal Shape Design of the S-Shaped Subsonic Intake Using NURBS. 43*rd AIAA Aerospace Sciences Meeting and Exhibit*, Reno, 10-13 January 2005, 455. https://doi.org/10.2514/6.2005-455

[13] Aranake, A., Lee, J.G., Knight, D., Cummings, R.M., Cox, J., Paul, M., *et al.* (2011) Automated Design Optimization of a Three-Dimensional Subsonic Diffuser. *Journal of Propulsion and Power*, **27**, 838-846. https://doi.org/10.2514/1.50522

[14] Zhang, Z. and Lum, K. (2006) S-Shaped Inlet Design Optimization Using the Adjoint Equation Method. 42*nd AIAA/ASME/SAE/ASEE Joint Propulsion Conference & Exhibit*, Sacramento, 9-12 July 2006, 4453. https://doi.org/10.2514/6.2006-4453

[15] Lee, B.J. and Kim, C. (2007) Automated Design Methodology of Turbulent Internal Flow Using Discrete Adjoint Formulation. *Aerospace Science and Technology*, **11**, 163-173. https://doi.org/10.1016/j.ast.2006.12.001

[16] Weske, J.R. (1943) Pressure Loss in Ducts with Compound Elbows. NACA Wartime Rept. W-39, National Advisory Committee for Aeronautics.

[17] Guo, R.W. and Seddon, J. (1982) An Investigation of the Swirl in an S-Duct. *Aeronautical Quarterly*, **33**, 25-58. https://doi.org/10.1017/s0001925900009288

[18] Goldsmith, E. and Seddon, J. (1993) Practical Intake Aerodynamic Design. Blackwell Scientific Publications.